Effect of $CePO_4$ on Structural, Magnetic and Optical Properties of Ceria Nanoparticles

Md. Abdullah Al Mamun [a, $], Manifa Noor [a, $], A. K. M. Atique Ullah [b], Md. Sarowar Hossain [c], Matin Md. Abdul [a], Md. Fakhrul Islam [a], M. A. Hakim [a]

[a] Department of Glass & Ceramic Engineering, Bangladesh University of Engineering & Technology, Dhaka 1000, Bangladesh

[b] Chemistry Division, Atomic Energy Center, Bangladesh Atomic Energy Commission, Dhaka 1000, Bangladesh

[c] S. N. Bose National Center for Basic Sciences, Salt Lake City, Kolkata, West Bengal 700098, India

[$] These authors contributed equally to the work

Corresponding Author: Md. Abdullah Al Mamun, mamun.mme@gmail.com

ABSTRACT. We report an intrinsic dilute ferromagnetism in CeO_2 nanoparticles prepared by a green synthesis route where *Artocarpus Heterophyllus* leaf extract is used as a bioreducing agent. PO_4^{3-} ions from leaf extract lock oxygen vacancy derived Ce^{3+} ions as $CePO_4$ at surface of the CeO_2 nanoparticles. The observed ferromagnetic behavior is strongly influenced by the distribution of frustrated Ce^{3+} ions at surface which has been attributed to the RKKY (Ruderman – Kittel – Kasuya – Yosida) type indirect exchange interaction of the spins. A giant redshift (~ 0.3 eV) in the optical bandgap with decrease in particle size indicates the presence of a spin polaron formed by the interaction between heavy fermion & charge carrier electrons in the system. The concept of locking the surface spins by phosphate ions may open up new possibilities for manipulation of the spin polarized charge carriers in future spintronics researches.

KEY WORDS. Dilute Magnetic Semiconductor, Spin Polaron, Green Synthesis.

Introduction

Weak ferromagnetism in nonmagnetic semiconductors has attracted a considerable interest in the field of spintronics due to the preservation of spin polarized charge carrieres. The concept of such dilute magnetic semiconductors (DMS) intially began with Mn doping in II–VI and III–V compounds which showed promising electrical, magnetic and optical properties but their curie temperature was much lower than room temperature ($T_C \approx 100$ K) [1 – 4]. After the groundbreaking experimental evidence of Co doped TiO_2 as DMS (T_C > RT), extensive researches on transition and rare earth metal doped nonmagnetic semiconductors have kept continuing [5]. Since then room temperature ferromagnetism has been found in doped TiO_2, ZnO, SnO_2, Cu_2O and $In_{1.8}Sn_{0.2}O_3$ [6 – 9]. But the concept of making DMS by doping of magnetic impurities was changed when room temperature ferromagnetism was observed in undoped nonmagnetic oxides like ZnO, TiO_2, In_2O_3, CeO_2 and HfO_2 [10 – 12]. The defects originated due to the synthesis process might be the reason for such intrinsic ferromagnetism in these materials but the true understanding of controlling the ferromagnetism to achieve desired spin injected electrical or optical properties remains still unclear.

Among these DMS candidates, CeO_2 steals the limelight for its unusual larger oxygen storage capacity and similar lattice parameter to Si. This transparent rare earth oxide is capable of having stable cubic structure up to ~50% defects as well as oxygen vacancies which enables this material to contain metal ions in a mixed valence state (Ce^{4+}/ Ce^{3+}) [13]. The oxygen vacancies, $V_{\ddot{O}}$ (Kroger – Vinger notation) leave e^- to its each neighbor Ce^{4+} and reduce them as Ce^{3+} ions [14]. The defect reaction for the formation of $V_{\ddot{O}}$ following Ce^{3+} is given as

$$2Ce_{Ce}^{x} + O_{O}^{x} = 2Ce_{Ce}^{\prime} + V_{\ddot{O}} + \frac{1}{2}O_2(gas) \ldots \ldots \ldots (1)$$

Recent reports highlighting the observation of both extrinsic and intrinsic ferromagnetism in CeO_2 have created a lot of enthusiasm in this field. Room temperature extrinsic ferromagnetism has been reported in Co, Fe, Cu, Gd and Mn doped CeO_2 [15 – 23] while numerous studies explored the intrinsic ferromagnetism of undoped CeO_2 in order to control the spin dependent electron transport system without the complicacy of any doping in the material. Sundaresan *et al.* stated that the exchange interaction between the unpaired spin of Ce^{3+} ions that result from surface oxygen vacancies is responsible for the origin of ferromagnetism in CeO_2 NPs [12]. Fernandes *et al.* identified this intrinsic ferromagnetism is vacancy dependent through experimental & theoretical approaches [24]. Chen *et al.* reported that ferromagnetism is oxygen vacancy dependent and increases with % Ce^{3+} ions but begins to decrease for excess amount of Ce^{3+} ions (~ 41%) at surface [25]. However, controversial claims have been also reported where researchers suggested that Ce^{3+}/Ce^{4+} concentration at surface is monotonically accountable for ferromagnetic behavior which has no relation with surface oxygen vacancies [26, 27].

In this work, green synthesis of CeO_2 nanoparticles (NPs) has been demonstrated using *Artocarpus Heterophyllus* leaf extract where $Ce(NO_3)_3.6H_2O$ was taken as Ce precursor. *Artocarpus Heterophyllus* is one of the most common trees found in the gardens in Southeast Asia and their evergreen leaf itself shows promising medicinal uses including antimicrobial, antifungal, anti-inflammatory, antioxidant activities [28]. Apart from the beneficial reasons of green synthesis like low process temperature, free of hazardous reagents and simple experimental setup, CeO_2 NPs synthesized by green synthesis route showed enhanced photoluminescent & antimicrobial activities [29 – 31]. This paper presents a straightforward approach of understanding the observed room temperature intrinsic ferromagnetic behavior in CeO_2 NPs by stabilizing the surface Ce^{3+} by PO_4^{3-} ions which comes from leaf extract. The experimental results indicate that the ferromagnetic behavior is strongly related with local spin density distribution at the surface. Furthermore, this investigation has found a possible correlation between ferromagnetic behavior and optical bandgaps of the CeO_2 NPs.

Experimental Section

Synthesis of Nanoparticles: Leaf extract was prepared which includes washing and drying of fresh green *A. Heterophyllus* leaves followed by blending to form fine powder. 10 gm leaf powder was then added in to 200 mL DI water and heated at 60 °C with continuous stirring for about 10 minutes. After filtration, the extract was collected for further purpose while $Ce(NO_3)_3.6H_2O$ was used as the precursor of Ce. 100 mL 0.01 M $Ce(NO_3)_3$ was added into 300 mL leaf extract and heated at 80 °C with continuous stirring until the dark brown gel formed. The gel was then dried at 120 °C for 12 hours and repeatedly centrifuged followed by drying to obtain the amorphous NPs. A detailed illustration of synthesis process is illustrated in **Figure 1**. Finally the samples were heat treated in air from 400 to 900 °C.

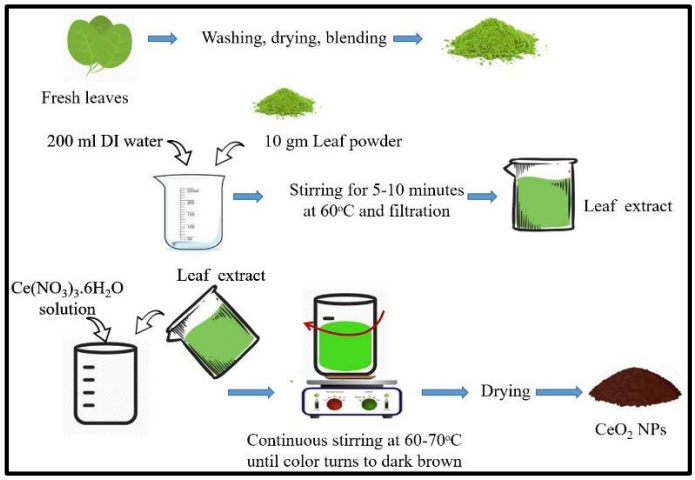

Figure 1. Green Synthesis of CeO_2 Nanoparticles

Characterization: Structural analysis of the annealed samples was carried out by X-Ray Diffraction (XRD) technique (Empyrean PANalytical-Netherlands) using CuKα radiation having wavelength 1.54 Å. Field Emission Scanning Electron Microscope (JSM, 7600 Jeol) was used to observe the morphology of the synthesized powders and to determine the elemental composition by Energy Dispersive X-ray Spectroscopy (EDS) analysis. Fourier Transform Infrared (FT-IR) spectroscopy (JASCO-FTIR-6300, Japan) was performed to determine the chemical bonds present both in leaf powder and annealed samples. Magnetization versus applied field up to 13.8 kOe was measured in 80, 200 and 300 K using Vibrating Sample Magnetometer (VSM) (Lakeshore 7407). The UV – Vis diffuse reflectance spectra of the samples were obtained using a UV-Vis spectrometer (UV/Vis/NIR – Lambda 1050, PerkinElmer, USA).

Results & Discussion

The X – Ray diffraction patterns of the CeO_2 NPs are presented in **Figure 2** which shows satisfactory correspondence with cubic fluorite structure (space group $Fm\bar{3}m$) of CeO_2. Presence of 2nd phase has been detected in all XRD patterns which are completely matched with monoclinic (space group *P 1 2₁/n*) Monazite – Ce phase. Rietveld refinement (**Figure 3**) was performed by Fullprof software which confirmed that $CePO_4$ phase formation has no significant dependence on annealing temperature. The phase fractions along with lattice parameters and crystallite size of CeO_2 phase of the samples which are annealed at 400 and 900 °C are listed in **Table 1**. Crystallite size of each sample was calculated using Scherrer's formula, $d = 0.9\lambda/\beta cos\theta$ where d is the crystallite size, β is the FWHM of diffraction peak (111), λ is the wavelength of X – Ray radiation and θ is the diffraction angle. The crystallite size increased from 3 nm to 23 nm due to the rise in the annealing temperature (400 °C to 900 °C).

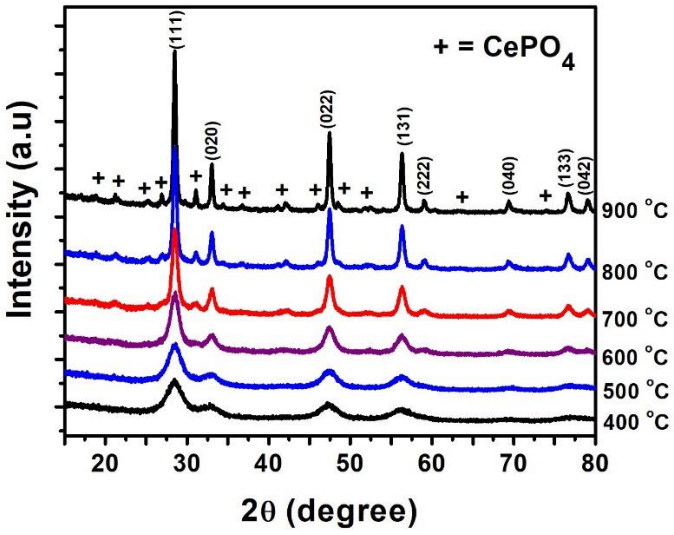

Figure 2. XRD Patterns of the samples annealed at different temperatures (400 – 900 °C).

Table 1: Structural parameters and crystallite size obtained from Rietveld Refinement of XRD Patterns

Sample	Phases Present	Unit Cell Parameters	Rietveld Factors	Crystallite Size of CeO_2 Phase (111 peak)
0.01 M 400 °C	CeO_2 76.82(68) % Cubic: $Fm\bar{3}m$ $CePO_4$ 23.18(41) % Monoclinic: *P1 2₁/n*	a = b = c = 5.432(0) Å V = 160.29(11) Å^3 a = 6.492(19) Å b = 8.228(19) Å c = 6.835(30) Å β = 115.63(28)º V = 329.17(97) Å^3	R_p = 19.8 R_{wp} = 20.1 R_{exp} = 16.6 χ^2 = 1.48	3 nm
0.01 M 500 °C	CeO_2 71.98(73) % Cubic: $Fm\bar{3}m$ $CePO_4$ 28.02(57) % Monoclinic: *P1 2₁/n*	a = b = c = 5.421(1) Å V = 159.36(8) Å^3 a = 6.838(17) Å b = 6.956(19) Å c = 6.273(16) Å β = 102.3(2)º V = 291.62(98) Å^3	R_p = 15.2 R_{wp} = 15.2 R_{exp} = 12.9 χ^2 = 1.4	5 nm
0.01 M 600 °C	CeO_2 69.02(49) % Cubic: $Fm\bar{3}m$ $CePO_4$ 30.98(36) % Monoclinic: *P1 2₁/n*	a = b = c = 5.414(0) Å V = 158.69(4) Å^3 a = 6.834(5) Å b = 7.015(6) Å c = 6.415(6) Å β = 103.43(2)º V = 299.88(45) Å^3	R_p = 18.7 R_{wp} = 17.1 R_{exp} = 13.7 χ^2 = 1.55	7 nm
0.01 M 700 °C	CeO_2 69.35(41) % Cubic: $Fm\bar{3}m$ $CePO_4$ 30.65(33) % Monoclinic: *P1 2₁/n*	a = b = c = 5.410(0) Å V = 158.35(2) Å^3 a = 6.801(2) Å b = 7.003(4) Å c = 6.474(3) Å β = 103.44(5)º V = 299.93(2) Å^3	R_p = 14.6 R_{wp} = 14.4 R_{exp} = 13.4 χ^2 = 1.16	11 nm
0.01 M 800 °C	CeO_2 69.34(68) % Cubic: $Fm\bar{3}m$ $CePO_4$ 30.66(37) % Monoclinic: *P1 2₁/n*	a = b = c = 5.409(0) Å V = 158.33(1) Å^3 a = 6.794(16) Å b = 7.017(20) Å c = 6.468(16) Å β = 103.44()º V = 299.95(13) Å^3	R_p = 16.5 R_{wp} = 15.9 R_{exp} = 13.3 χ^2 = 1.42	16 nm
0.01 M 900 °C	CeO_2 68.11(71) % Cubic: $Fm\bar{3}m$ $CePO_4$ 31.89(73) % Monoclinic: *P1 2₁/n*	a = b = c = 5.409(0) Å V = 158.31(0) Å^3 a = 6.791(0) Å b = 7.009(2) Å c = 6.469(0) Å β = 103.44(2)º V = 299.58(11) Å^3	R_p = 20.2 R_{wp} = 19.4 R_{exp} = 13.3 χ^2 = 2.13	23 nm

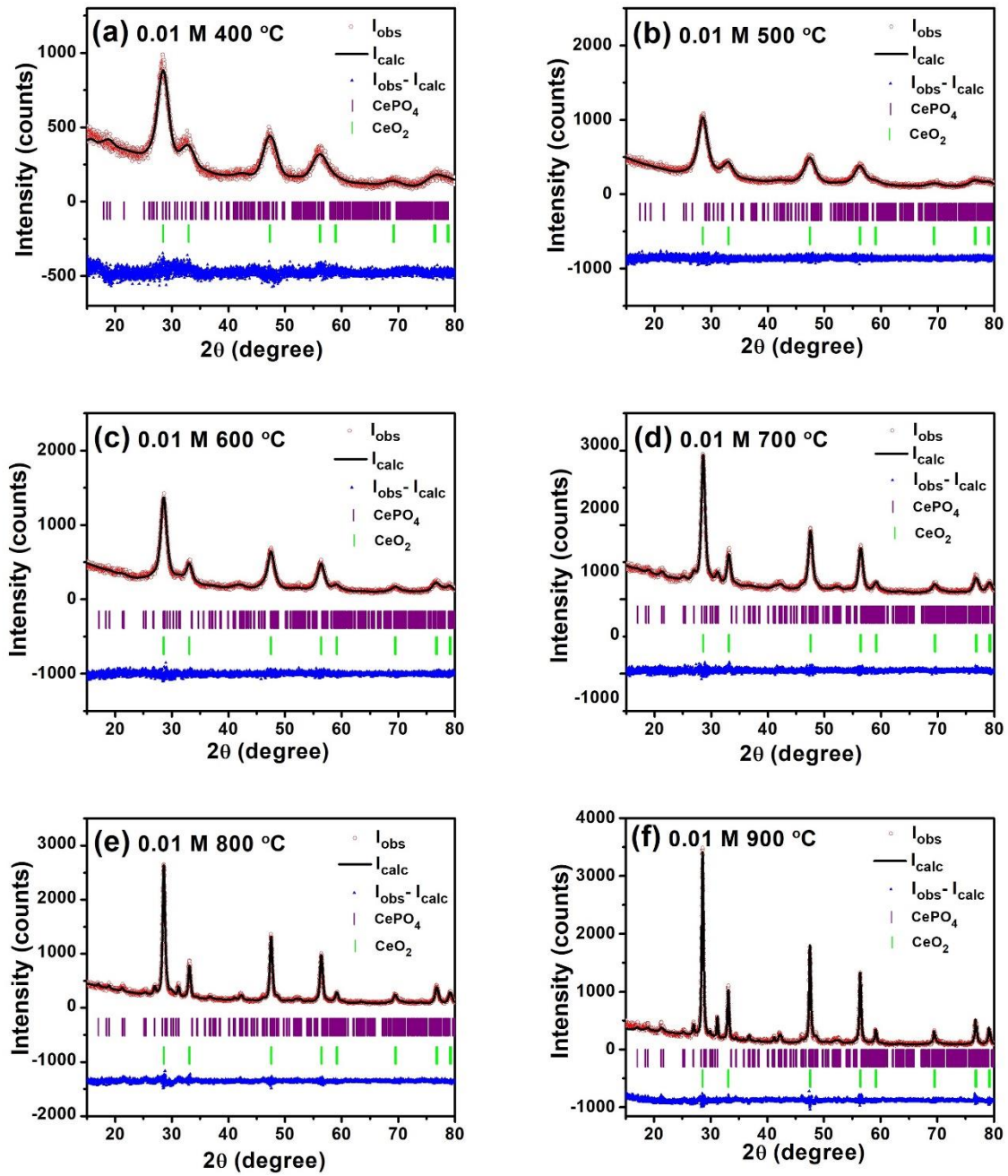

Figure 3. Fitting patterns obtained after Rietveld refinement showing Bragg positions of CeO_2 and $CePO_4$ Phase in 0.01 M samples annealed at 400 – 900 °C (a – f).

The formation of $CePO_4$ phase during synthesis of CeO_2 is quite interesting and we attribute it to be related with the oxygen vacancy in our study. Due to the large surface to bulk ratio, the Ce^{3+} originated from the oxygen vacancies can be considered as the surface atoms in the CeO_2 NPs (~20 nm). These Ce^{3+} later attracts the PO_4^{3-} ions of leaf extract and yield $CePO_4$ phase (as illustrated in **Figure 4**). The presence of PO_4^{3-} ions in *Artocarpus Heterophyllus* leaf is confirmed by GC – MS (Gas Chromatography – Mass Spectroscopy) of leaf extract (provided in **Electronic Supplementary Information**).

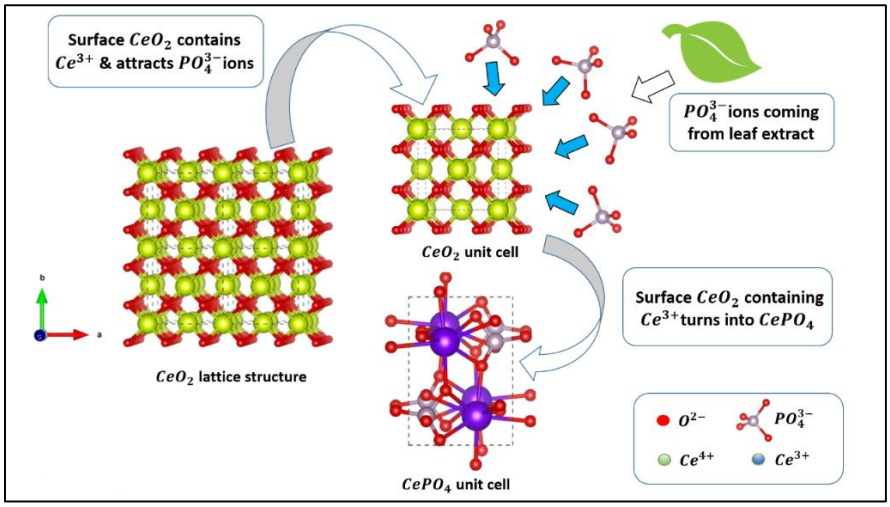

Figure 4. Schematic illustration of CeO_2 – $CePO_4$ in the samples

This phosphate ions derived $CePO_4$ phase in CeO_2 has been observed earlier by Singh *et al.* where they showed that formation of $CePO_4$ phase leads a significant loss in catalytic behavior of CeO_2 NPs [32]. Since the catalytic behavior is strongly related to the oxygen vacancy storage capacity of CeO_2 NPs, our intuitive explanation that oxygen vacancy derived surface Ce^{3+} attracts the PO_4^{3-} ions from leaf extract and form $CePO_4$ phase is in good agreement with the literature.

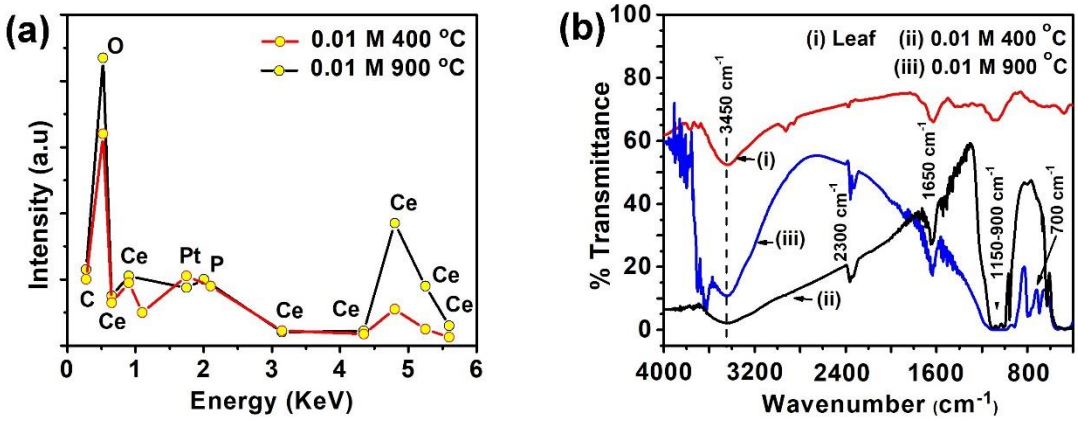

Figure 5. (a) EDS and (b) FTIR spectra of samples & leaf.

Presence of $CePO_4$ phases is further confirmed by EDS (**Figure 5 a**) & FTIR (**Figure 5 b**) analysis of the samples. The absorbtion peaks at 3650 – 3150 cm^{-1} and 1650 cm^{-1} indicates streching of O–H bonds of water molecules and asymmetric streching of C=O bonds respectively [33, 34]. Assymetric strecthing and bending of P–O bonds have been observed at 1140 – 990 cm^{-1} which confirms the presence of PO_4^{3-} in the NPs [35, 36]. The absorption peaks below 700 cm^{-1} can be attributed to the strecthing of Ce–O bonds [34].

Figure 6 shows the magnetization vs. magnetic field plots measured at 80, 200 and 300 K while relevant parameters are listed in **Table 2**. In 0.01 M 900 °C sample, saturation magnetization values are found higher than in 0.01 M 400 °C sample. The change of hysteresis loop with decrease in temperature (300 to 80 K) maybe a result of the competing interactions between ferromagnetic and antiferromagnetic behavior of the Ce^{3+} spins. Prior that it is noteworthy to elucidate the contribution

of CeO_2 and $CePO_4$ phases to the ferromagnetism in the synthesized samples. The surface oxygen vacancy derived Ce^{3+} ions are the key reason for origin of ferromagnetism in pure CeO_2 and in our synthesized samples, the CeO_2 phase does not contain such Ce^{3+} ions as they are already stabilized as $CePO_4$ on the surface of CeO_2 nanoparticles. So in a broad sense, the four Ce^{3+} ions in monoclinic $CePO_4$ crystal structure are responsible for the observed ferromagnetism in our samples which were originated from oxygen vacancies in CeO_2 NPs.

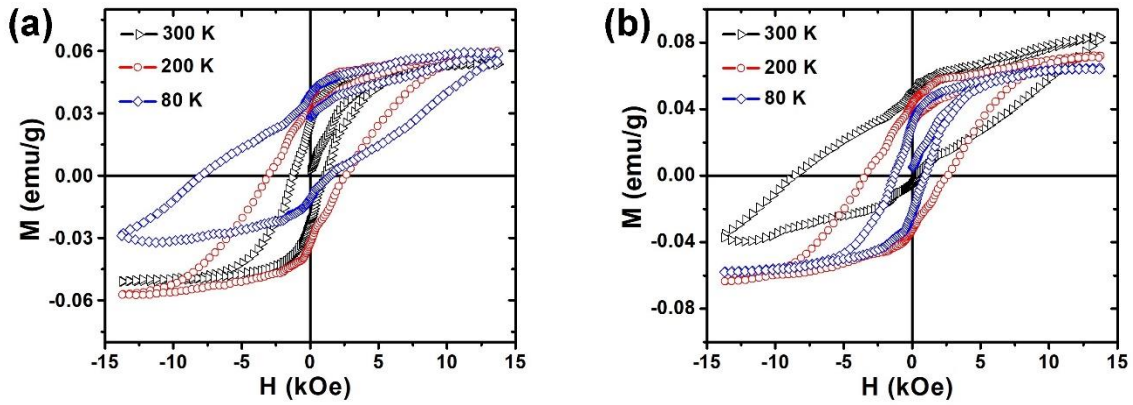

Figure 6. Magnetization vs. field plots of (a) 0.01 M 400 °C and (b) 0.01 M 900 °C sample measured at 80, 200 and 300 K.

Table 2: Magnetic parameters extracted from **Figure 6** (a) and (b)

CeO_2 (0.01) (400 °C)			
	300 K	200 K	80 K
H_C	1280 Oe	3062 Oe	7972 Oe
M_R	0.026 (emu/g)	0.037 (emu/g)	0.039 (emu/g)
M_S	0.05 (emu/g)	0.059 (emu/g)	0.058 (emu/g)
CeO_2 (0.01) (900 °C)			
H_C	8583 Oe	3418 Oe	1335 Oe
M_R	0.049 (emu/g)	0.043 (emu/g)	0.031 (emu/g)
M_S	0.083 (emu/g)	0.071 (emu/g)	0.064 (emu/g)

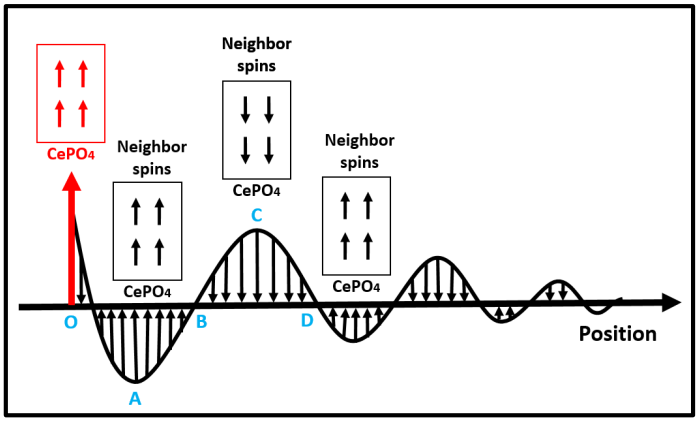

Figure 7. RKKY Coupling of Ce^{3+} ions

At first look, this ferromagnetism appears to be unusual as saturation magnetization was found decreasing from 0.083 emu/g to 0.05 emu/g with decrease in crystallite size (23 nm to 3 nm). Although the size dependent ferromagnetism has been reported in many previous studies where researchers suggest that saturation magnetization should be increasing with decrease in crystallite size in nanoscale range because large surface to volume ratio ensures the possibility of having more oxygen vacancies at surface [12, 37]. In our study, the unusual relation between the crystallite size & saturation magnetization M_s can be attributed to the RKKY (Ruderman – Kittel – Kasuya – Yosida) coupling of Ce^{3+} ions. The spins located in any single $CePO_4$ crystal are well polarized and act as a single spin. This single spin mediates its neighbor spins which decays as an algebraic way in terms of distance between themselves (illustrated as **Figure 7**). In the 3 nm crystallite size samples, this indirect exchange interaction favors antiferromagnetism which is the main reason of the reduced net ferromagnetism in the 400 °C annealed samples. Similarly due to much flexibility in local spin density, increased net ferromagnetism has been observed in 900 °C annealed samples (23 nm crystallite size).

The optical absorption properties were investigated from Diffuse Reflectance spectra of the annealed samples showing in **Figure 8**. The samples exhibit reflectance peaks with a slight change in reflectance (1 – 1.5%) at 270 nm and 340 nm which are due to the charge transfer transition from valence band O^{2-} 2p to conduction band Ce^{4+} 4f orbitals [38, 39]. Optical band gaps of the samples can be estimated from the following expression proposed by Tauc where $n = 2$ & $^1/_2$ for indirect and direct bandgaps respectively [40].

$$(\alpha h\vartheta)^{\frac{1}{n}} = A(h\vartheta - E_g) \dots\dots\dots\dots (2)$$

Here, A is the proportional constant and α is the absorption coefficient which can be written as Kubelka – Munk function $F(R) = \frac{(1-R)^2}{2R}$ where R is the reflectance found for the samples. So, substituting α with $F(R)$ in the equation (2):

$$[F(R)h\vartheta]^{\frac{1}{n}} = A(h\vartheta - E_g) \dots\dots\dots\dots (3)$$

For $n = {}^1/_2$, we have found a sharp and straight fall of graph which revealed that all our samples have direct bandgap. So, the slope on the $[F(R)h\vartheta]^2$ vs. photon energy (E) graph cuts x axis at $[F(R)h\vartheta]^2 = 0$ which gives the bandgap E_g of the particular sample. The bandgap found for the samples are shown in **Figure 8**.

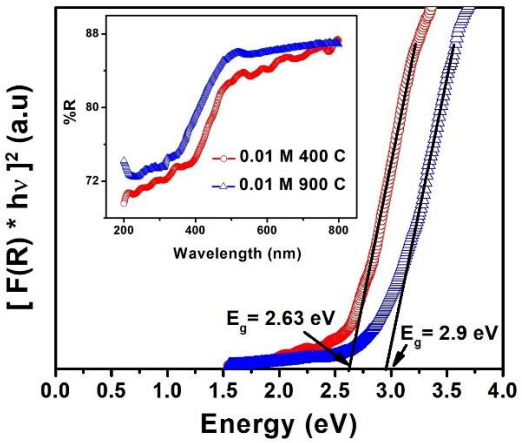

Figure 8. Diffused reflectance spectra (inset) and Bandgaps of 0.01 M samples annealed at 400 °C and 900 °C.

Unlike the conventional quantum confinement effect in NPs, our study exhibits giant red shifts (~ 0.3 eV) in the bandgap with decrease in size. Previous studies suggest that concentration of Ce^{3+} is related to the unusual red shift in band gap of CeO_2 NPs [41]. Chowdhury *et al.* attributed the red shifting of indirect bandgap to the interfacial polaron effect due to electron – phonon coupling [42]. As all of our samples exhibit direct bandgaps, we assume that electron – phonon interaction should not have significant influence on the observed red shift in bandgaps. Instead of e^- – phonon interaction, we bring a concept of interaction between charge carrier electrons & heavy fermions ($4f^1$) of Ce^{3+} ions to explain the observed red shift in the bandgap. While being in a same lattice, the charge carrier e^- & heavy fermion creates a spin polaron. Due to the heavy fermion contribution, the electronic mobility of this polaron decreases and spin magnitude increases. In our experiment, the samples annealed at 900 °C exhibit higher ferromagnetism (M_S) & bandgap (0.083 emu/g & 2.9 eV) compared to the samples annealed at 400 °C (0.05 emu/g & 2.63 eV) which supports our elucidation that the giant redshift is strongly attributed to the spin mediated optical properties of the NPs.

Conclusions

In this work, CeO_2 NPs are obtained from a simple green synthesis route which uses *A. Heterophyllus* leaf extract as bioreducing agent. Room temperature ferromagnetism has been found decreasing as particle size is reduced from 23 nm to 3 nm which indicates that the behavior of frustrated Ce^{3+} spins at surface is strongly dominated by RKKY type indirect exchange interaction mechanism. A giant red shift (~ 0.3 eV) in the direct bandgaps with decrease in particle size consolidates the intuition that the presence of spin polarons might be the controlling factor of the optical properties of CeO_2 NPs. Having in mind that before considering CeO_2 for designing novel spintronics devices, the distribution of disordered surface spins needs an exclusive treatment from both experimental and theoretical viewpoints and we believe this research will provide beneficial insights to DMS community.

Conflicts of Interest

There are no conflicts to declare.

Acknowledgements

The authors would like to thank the Bangladesh University of Engineering and Technology (BUET), Atomic Energy Center, Dhaka and S. N. Bose National Center for Basic Sciences, Kolkata, India for providing assistance regarding synthesis & characterization of the samples.

Electronic Supplementary Information

Gas Chromatography – Mass Spectroscopy (GC – MS) data of leaf extract and Field Emission Scanning Electron Microscopy (FESEM) images of synthesized nanoparticles.

References

1) J. K. Furdyna. **J. Appl. Phys. 64**, R29 (1988).
2) H. Munekata *et al*. (1989). Diluted Magnetic III-V Semiconductors. **Phys. Rev. Lett. 63**, 1849.
3) D. Ferrand, J. Cibert, A. Wasiela, C. Bourgognon, S. Tatarenko, and G. Fishman. **Phys. Rev. B. 63,** 085201 (2001).
4) K.W. Edmonds *et al*. (2002). High Curie temperature $Ga_{1-x}Mn_xAs$ obtained by resistance-monitored annealing. **Appl. Phys. Lett. 81**, 4991.
5) Yuji Matsumoto, Makoto Murakami, Tomoji Shono, Tetsuya Hasegawa, Tomoteru Fukumura, Masashi Kawasaki, Parhat Ahmet, Toyohiro Chikyow, Shin-ya Koshihara, Hideomi Koinuma. **Science. 291**, 854 (2001)
6) J. B. Yi, C. C. Lim, G. Z. Xing, H. M. Fan, L. H. Van, S. L. Huang, K. S. Yang, X. L. Huang, X. B. Qin, B.Y. Wang, T. Wu, L. Wang, H. T. Zhang, X.Y. Gao, T. Liu, A. T. S. Wee, Y. P. Feng, and J. Ding. **Phys. Rev. Lett. 104**, 137201 (2010).
7) Kenji Ueda, Hitoshi Tabata, and Tomoji Kawai. **Appl. Phys. Lett. 79**, 988 (2001).
8) S. B. Ogale *et al*. (2003). High Temperature Ferromagnetism with a Giant Magnetic Moment in Transparent Co-doped $SnO_{2-\delta}$. **Phys. Rev. Lett. 91**, 077205.
9) John Philip, Nikoleta Theodoropoulou, Geetha Berera, Jagadeesh S. Moodera, and Biswarup Satpati. **Applied Physics Letters. 85**, 777 (2004).
10) Nguyen Hoa Hong *et al*. (2006) Room-temperature ferromagnetism observed in undoped semiconducting and insulating oxide thin films. **Phys. Rev. B. 73**, 132404.
11) M. Venkatesan *et al.* (2004) Thin films: unexpected magnetism in a dielectric oxide. **Nature. 430** (7000), 630.
12) A. Sundaresan *et al.* (2006) Ferromagnetism as a universal feature of nanoparticles of the otherwise nonmagnetic oxides. **Phys. Rev. B. 74**, 161306(R).
13) P R L Keating *et al.* (2009) Intrinsic ferromagnetism in CeO_2: dispelling the myth of vacancy site localization mediated superexchange. **J. Phys.: Condens. Matter. 21**, 405502.
14) N.V. Skorodumova, S. I. Simak, B. I. Lundqvist, I. A. Abrikosov, and B. Johansson. **Phys. Rev. Lett. 89**, 166601 (2002).
15) A. Bouaine, R. J. Green, S. Colis, P. Bazylewski, G. S. Chang, A. Moewes, E. Z. Kurmaev, and A. Dinia. **J. Phys. Chem. C. 115**, 1556–1560 (2011).
16) HS Saini, M Singh, AH Reshak, MK Kashyap. **Computational Materials Science. 74,** 114–118 (2013)
17) M. S. Seehra *et al.* (2012) Effects of Cu doping on the magnetism of CeO_2 nanoparticles. **Journal of Applied Physics. 111,** 07B516.
18) Gao-Ren Li *et al.* (2009) Hierarchically Porous Gd^{3+}-Doped CeO_2 Nanostructures for the Remarkable Enhancement of Optical and Magnetic Properties. **J. Phys. Chem. C. 113**, 1235–1241.
19) Chuanhui Xia *et al.* (2010) Magnetic properties and photoabsorption of the Mn-doped CeO_2 nanorods. **Materials Research Bulletin. 45**, 794–798.

20) Anita M. D'Angelo, Alan L. Chaffee, **ACS Omega 2**, 2544−2551 (2017).
21) Pawan Kumar *et al.* "Enhancement of ferromagnetism in C ion implanted CeO_2 thin films" **Mater. Res. Express 4**, 036403 (2017).
22) Y Wu *et al.* "Microstructure and ferromagnetism of Co-doped CeO_2 nano-octahedrons" **Materials Letters 183,** 161–164 (2016).
23) H.F Xu *et al.* "The effect of Co-doped on the room-temperature ferromagnetism of CeO_2 nanorods" **Journal of Magnetism and Magnetic Materials 377**, 272–275 (2015).
24) V. Fernandes *et al*. (2009) Dilute-defect magnetism: Origin of magnetism in nanocrystalline CeO_2. **Phys. Rev. B. 80**, 035202.
25) SY Chen, CH Tsai, MZ Huang, DC Yan, TW Huang, A Gloter, CL Chen, HJ Lin, CT Chen, and CL Dong. **J. Phys. Chem. C. 116**, 8707−8713 (2012).
26) Yinglin Liu *et al*. (2008) Size dependent ferromagnetism in cerium oxide (CeO_2) nanostructures independent of oxygen vacancies. **J. Phys.: Condens. Matter. 20,** 165201 (5pp).
27) M Li *et al*. (2009) Relationship between the surface chemical states and magnetic properties of CeO_2 nanoparticles. **Appl. Phys. Lett. 94**, 152511.
28) Om Prakash, Rajesh Kumar, Anurag Mishra, Rajiv Gupta. **Phcog Rev. 3**, 353-358 (2009).
29) J. Malleshappa *et al*. (2014) Eco-friendly green synthesis, structural and photoluminescent studies of CeO_2:Eu^{3+} nanophosphors using E.tirucalli plant latex. **Journal of Alloys and Compounds. 612,** 425 – 434.
30) KM Kumar *et al*. (2017). Green synthesis of Ce^{3+} rich CeO_2 nanoparticles and its antimicrobial studies. **Materials Letters. 214**, 15 – 19.
31) Santi Maensiri, Sarawuth Labuayai, Paveena Laokul, Jutharatana Klinkaewnarong, and Ekaphan Swatsitang. **Japanese Journal of Applied Physics. 53**, 06JG14 (2014).
32) Sanjay Singh, Talib Dosani, Ajay Karakoti, Amit Kumar, Sudipta Seal, and William T. Self. **Biomaterials. 32** (28): 6745–6753 (2011).
33) Guofeng Wang *et al.* (2010). Synthesis, characterization and photoluminescence of CeO_2 nanoparticles by a facile method at room temperature. **Journal of Alloys and Compounds. 493**, 202–207.
34) Mahmuda Akter *et al*. (2018). *Brassica rapa* var. *japonica* Leaf Extract Mediated Green Synthesis of Crystalline Silver Nanoparticles and Evaluation of Their Stability, Cytotoxicity and Antibacterial Activity. **Journal of Inorganic and Organometallic Polymers and Materials. 28,** 1483–1493.
35) D. Palma-Ramírez, M.A. Domínguez-Crespo, A.M. Torres-Huerta, H. Dorantes-Rosales, E. Ramírez-Meneses, E. Rodríguez. **Journal of Alloys and Compounds. 643**, S 209 – S 218 (2014).
36) Nuengruethai Ekthammathat, Titipun Thongtem, Anukorn Phuruangrat, and Somchai Thongtem. **Journal of Nanomaterials**. 958593 (2012).
37) Mehedi Hasan, M. A. Hakim, M. A. Basith, Md. Sarowar Hossain, Bashir Ahmmad, M. A. Zubair, A. Hussain, and Md. Fakhrul Islam. **AIP Advances. 6**, 035314 (2016).
38) Chunman Ho, Jimmy C. Yu, Tszyan Kwong, Angelo C. Mak, and Sukyin Lai. **Chem. Mater. 17**, 4514-4522 (2005).
39) Zhenling Wang *et al.* (2007) Remarkable Changes in the Optical Properties of CeO_2 Nanocrystals Induced by Lanthanide Ions Doping. **Inorg. Chem. 46**, 13, 5237-5242.
40) Li Li, Haoran Wang, Lei Zou and Xiong Wang. **RSC Adv. 5**, 41506-41512 (2015).
41) Mohammad Mansoob Khan, Sajid Ali Ansari, Debabrata Pradhan, Do Hung Han, Jintae Lee, and Moo Hwan Cho. **Ind. Eng. Chem. Res. 53**, 9754−9763 (2014).
42) Biswajit Choudhury, Amarjyoti Choudhury. **Materials Chemistry and Physics. 131**, 666– 671 (2012).

Figures

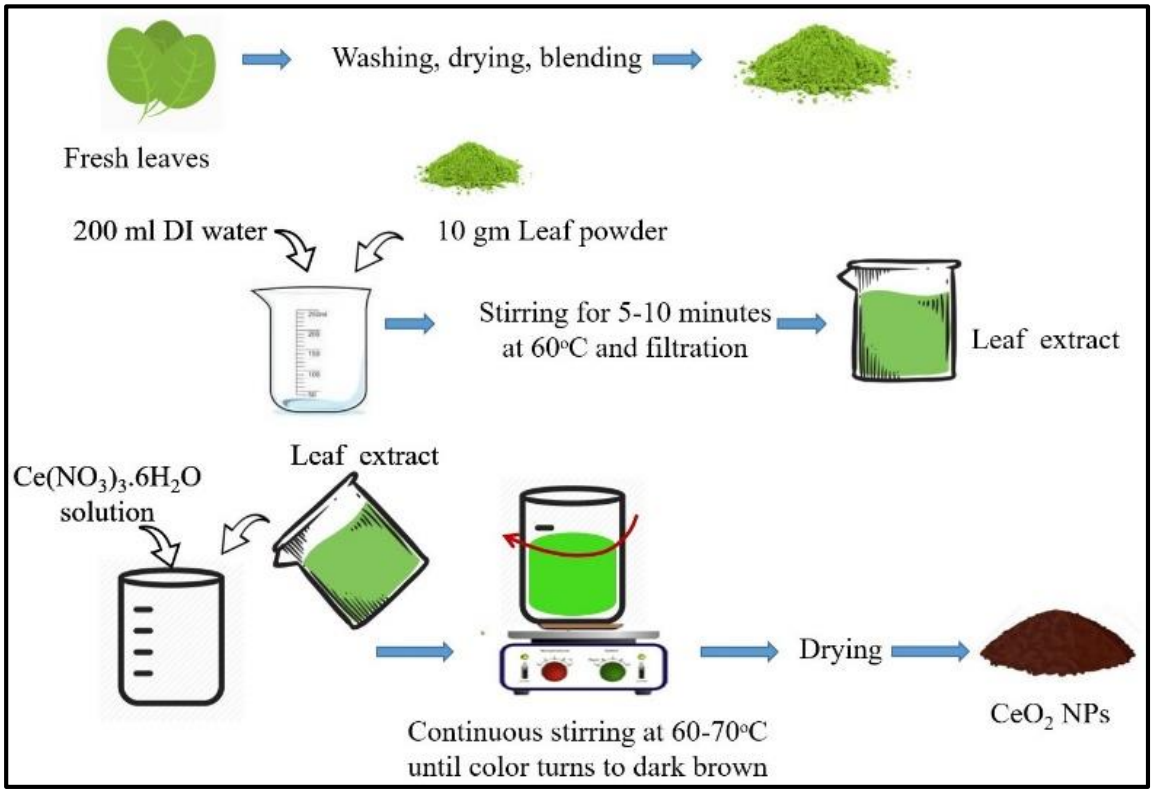

Figure 1. Green Synthesis of CeO_2 Nanoparticles

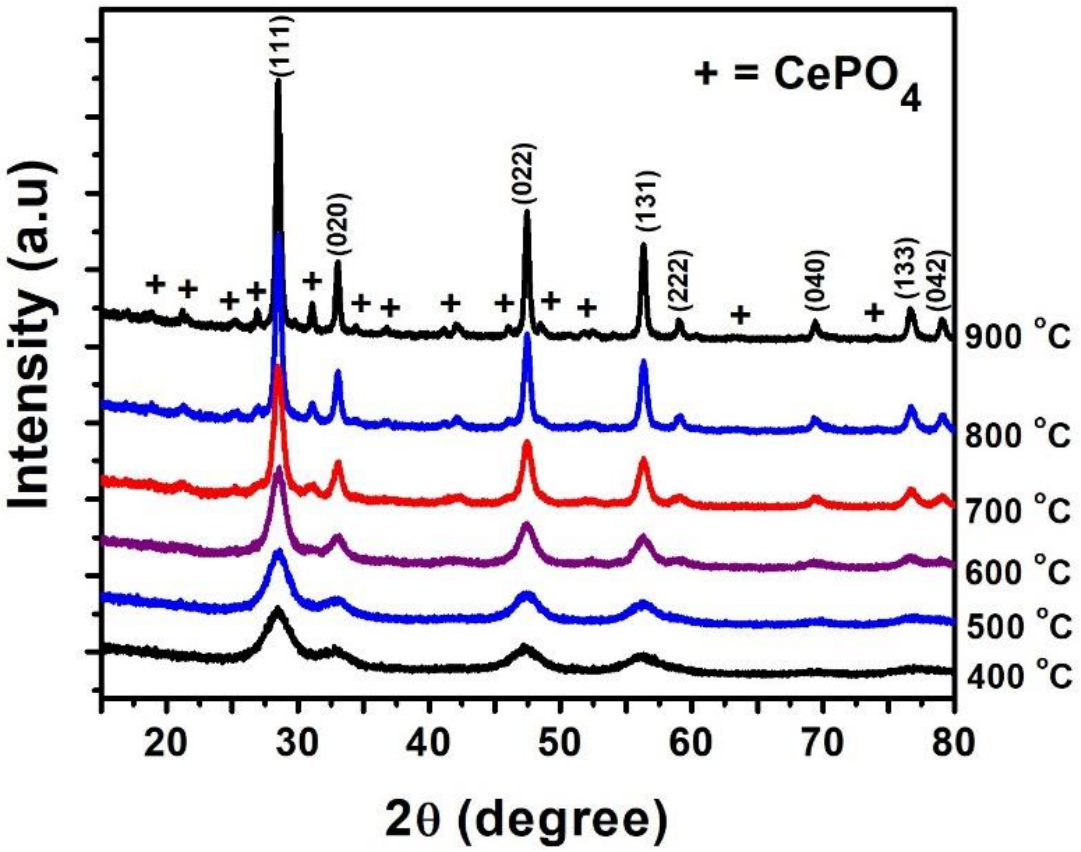

Figure 2. XRD Patterns of the samples annealed at different temperatures (400 – 900 °C).

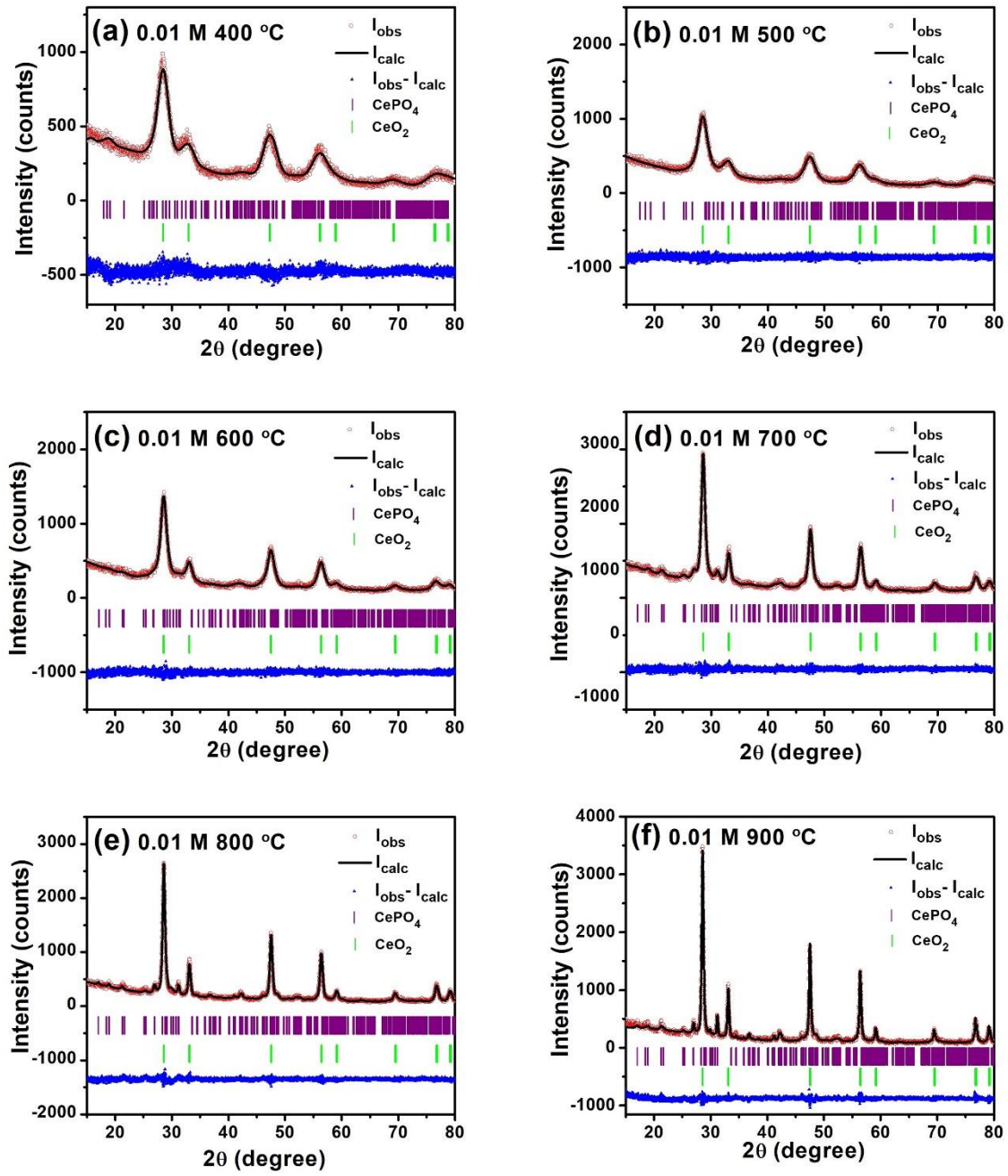

Figure 3. Fitting patterns obtained after Rietveld refinement showing Bragg positions of CeO_2 and $CePO_4$ Phase in 0.01 M samples annealed at 400 – 900 °C (a – f).

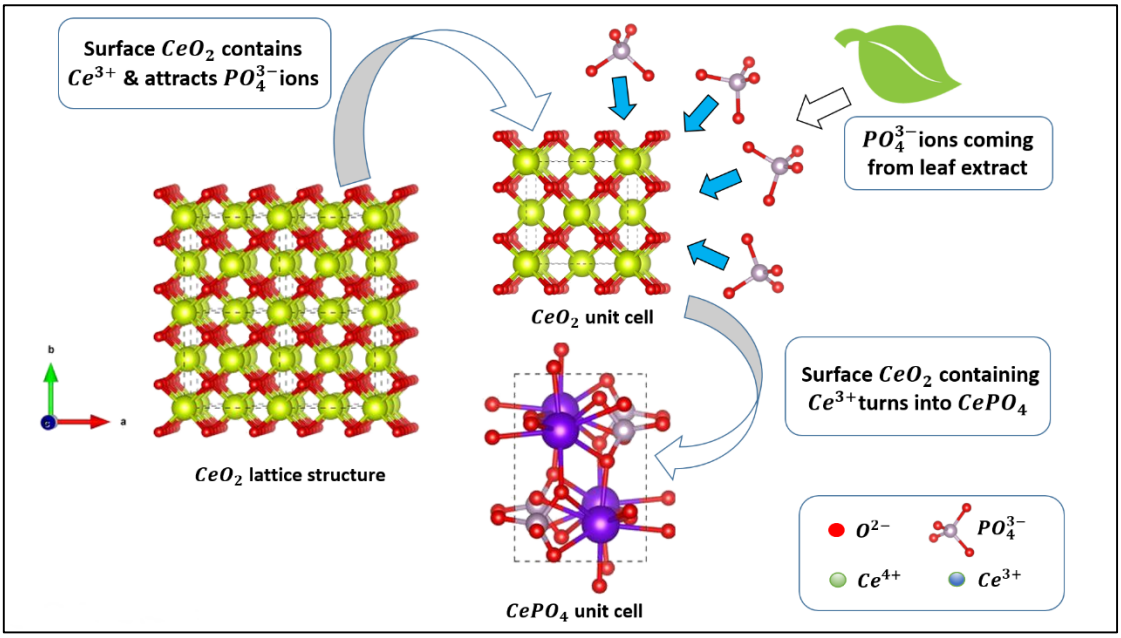

Figure 4. Schematic illustration of CeO_2 – $CePO_4$ in the samples

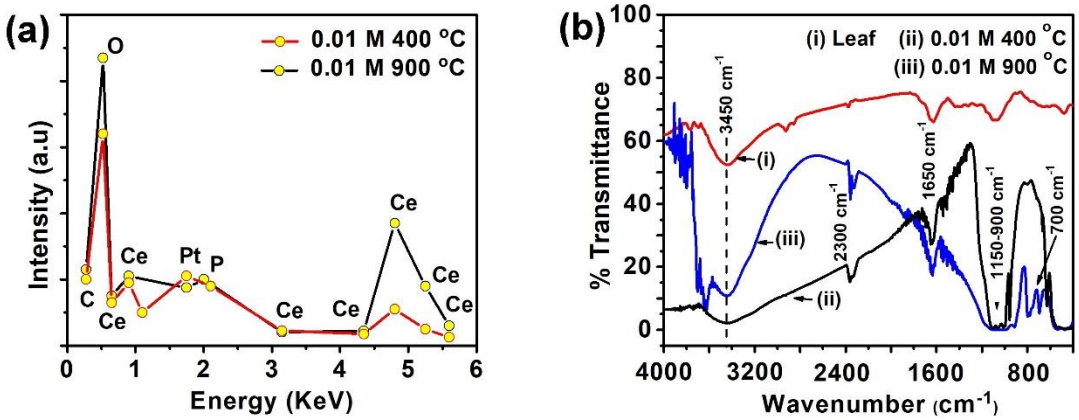

Figure 5. (a) EDS and (b) FTIR spectra of samples & leaf.

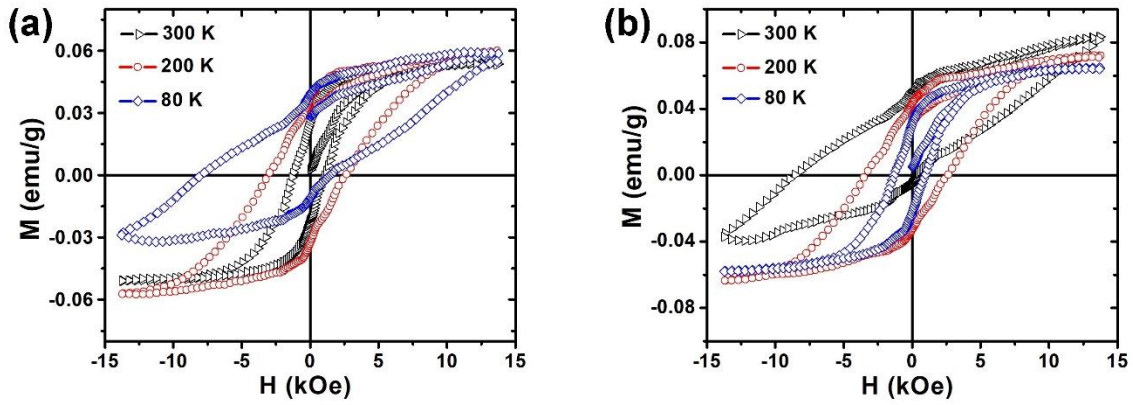

Figure 6. Magnetization vs. field plots of (a) 0.01 M 400 °C and (b) 0.01 M 900 °C sample measured at 80, 200 and 300 K.

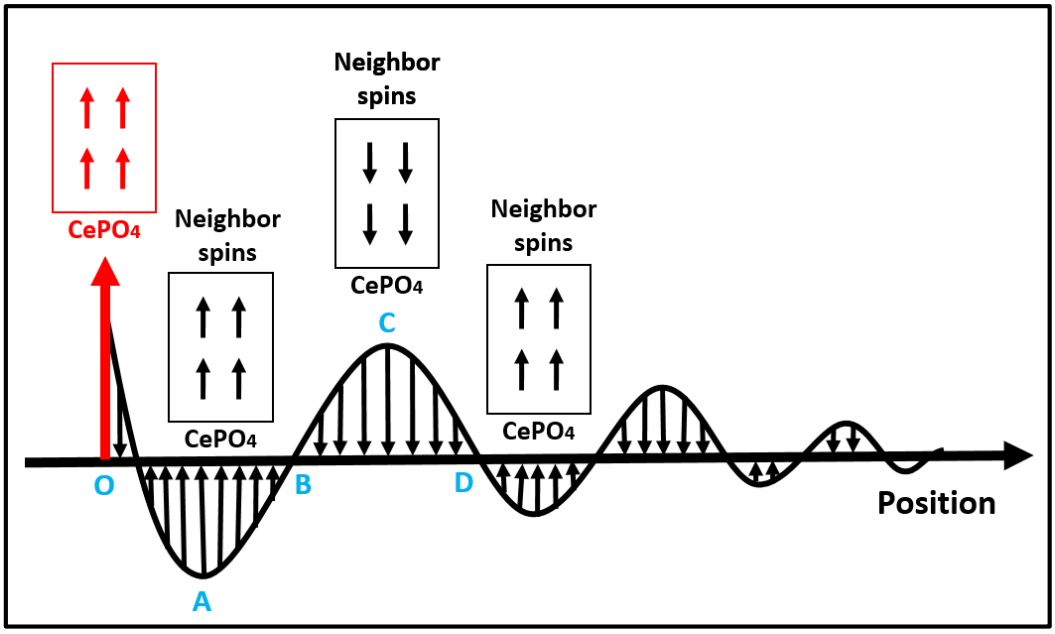

Figure 7. RKKY Coupling of Ce^{3+} ions

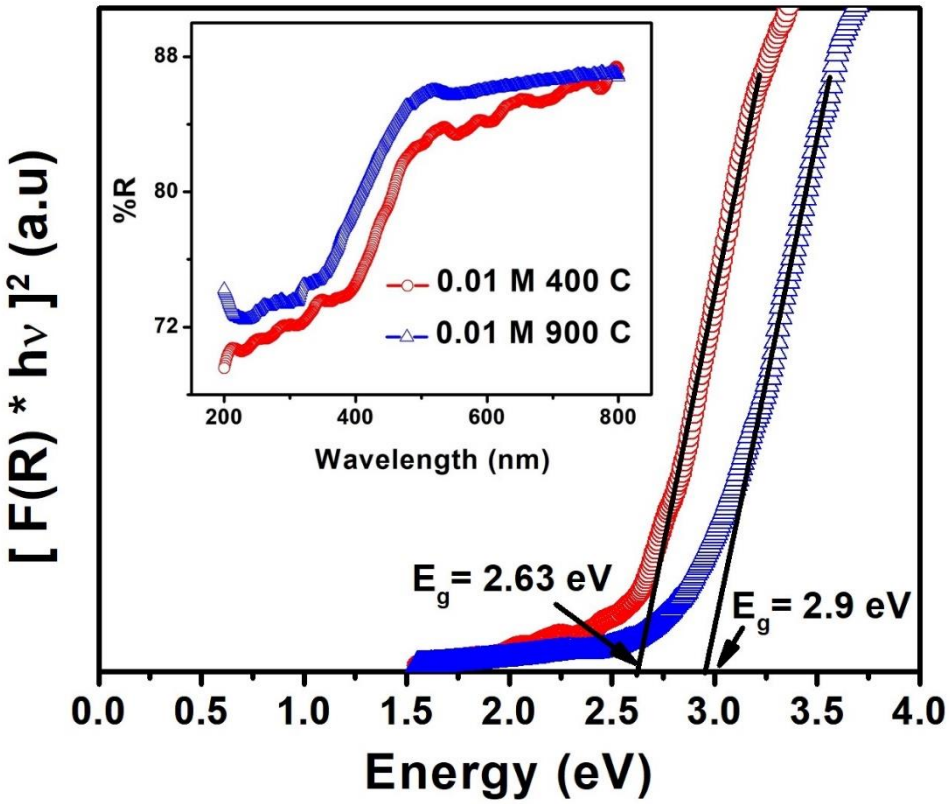

Figure 8. Bandgaps and (inset) Diffused reflectance spectra of 0.01 M samples annealed at 400 °C and 900 °C.